Author's personal copy

Journal of Alloys and Compounds 579 (2013) 138–146

Contents lists available at SciVerse ScienceDirect

Journal of Alloys and Compounds

journal homepage: www.elsevier.com/locate/jalcom

Phase transformation and precipitation of an Al–Cu alloy during non-isothermal heating studied by in situ small-angle and wide-angle scattering

Cheng-Si Tsao [a,*], E-Wen Huang [b,*], Ming-Hsien Wen [b], Tsung-Yuan Kuo [c], Sheng-Long Jeng [a], U-Ser Jeng [d], Ya-Sen Sun [b]

[a] Institute of Nuclear Energy Research, Longtan, Taoyuan 32546, Taiwan
[b] Department of Chemical and Materials Engineering and Center for Neutron Beam Applications, National Central University, Taoyuan 32001, Taiwan
[c] Department of Mechanical Engineering, Southern Taiwan University of Science and Technology, Tainan 71005, Taiwan
[d] National Synchrotron Radiation Research Center, Hsinchu 30077, Taiwan

ARTICLE INFO

Article history:
Received 10 March 2013
Received in revised form 27 April 2013
Accepted 29 April 2013
Available online 16 May 2013

Keywords:
Al–Cu alloy
Precipitation
Phase transformation
Small-angle X-ray scattering
Wide-angle X-ray scattering

ABSTRACT

Understanding the classic precipitation sequence of Al–Cu alloys, solid solution → Guinier–Preston (GP) zones → θ″ → θ′ → stable θ, is of academic importance. In situ synchrotron small-angle X-ray scattering (SAXS) and wide-angle X-ray scattering (WAXS) techniques were employed simultaneously to study the temperature-dependent behavior of various intermediate precipitation steps in the non-isothermal heating of Al–5.4 wt%Cu alloy. This study quantitatively demonstrates the concurrent evolution of the lattice structure, volume fraction (growth and dissolution) and structural growth in the thickness and length directions with temperature for various intermediate (metastable) precipitates for the first time. The detailed phase transformation mechanism and structural evolution in the precipitation sequence (for GP zones, θ″, θ′ and θ phases) can then be resolved. Our data analysis also considered the concurrent existence of multiple precipitates in the precipitation sequence. Moreover, the evolutional behavior of the orientation of precipitates in each precipitation step can be concurrently revealed. Different SAXS analysis models were proposed to successfully interpret the SAXS data. The new information presented by the SAXS/WAXS approach provides insight into the phase transformation mechanism of precipitation in Al–Cu alloys.

© 2013 Elsevier B.V. All rights reserved.

1. Introduction

Aluminum alloys have potential applications in various vehicles and portable devices due to their low weight and high strength. Precipitation hardening by heat treatment is critical in optimizing mechanical performance to achieve rational design. Al–Cu alloys, with metastable and spatially dispersed θ′ precipitates as the primary strengthening phase, have a long history and are of academic importance [1–9]. The θ′ phase of Al–Cu alloys has been a favorite model system for studying the theories or mechanisms of phase transformation in aluminum alloys [2]. The well-known classical precipitation sequence during heating, solid solution (SS) → Guinier–Preston (GP) zones (or GP I zones) → θ″ (or GP II zones) → θ′ → stable θ, is the textbook example of aging hardening [1–3]. The nucleation and growth of θ′ precipitates is arguably the model case for understanding the transition of intermediate (metastable) phases starting from the decomposition of a supersaturated solid solution. The formation and structure of metastable GP and θ″ (GP II) zones in the Al–Cu alloys has also attracted fundamental research interest [4,7,10–13].

Although extensive experimental studies have been conducted on the various precipitates in Al–Cu alloys, they focused on the lattice structures, interfacial characteristics and nanoscale morphology of precipitates using transmission electron microscopy (TEM) [2,4–7,13,14], atom-probe tomography [3] and X-ray diffraction, among other techniques. Several theoretical studies have also been conducted on the growth kinetics, morphology and strengthening mechanism of θ′ phase [1,8,9]. However, due to the lack of accurate information, such as the chemical free energies of metastable phases, lattice mismatch on the interface, interfacial energies and elastic strain, the development of model calculations has also focused on the θ′ phase under a certain set of simplified conditions [1,2]. On the other hand, microscopic observations have inherent drawbacks, such as limited sample preparation, local variation and counting statistics. Comprehensive quantitative or

* Corresponding authors. Tel.: +886 3 4711400x3420; fax: +886 3 4115851 (C.-S. Tsao), tel.: +886 3 4227151x34207 (E.-W. Huang).
E-mail addresses: cstsao@iner.gov.tw (C.-S. Tsao), ewhuang@ncu.edu.tw (E.-Wen Huang).

0925-8388/$ - see front matter © 2013 Elsevier B.V. All rights reserved.
http://dx.doi.org/10.1016/j.jallcom.2013.04.201

Author's personal copy

qualitative understanding of the phase transformation between the intermediate phases and complex structural evolution in this precipitation sequence is still lacking. So far, no experimental work has simultaneously measured both the phase (lattice structure) transformation and the morphological evolution (including the growth and dissolution of the volume fraction) of various intermediate phases in the precipitation sequence for Al–Cu alloys. Differential scanning calorimetry (DSC) can be used to effectively investigate the precipitation kinetics (relative volume fraction) or qualitative temporal behavior of the precipitation sequence [15–19]. This method is based on simplified assumptions and previously known information. The non-isothermal theoretical model was developed simply based on the response of a metastable phase into stable phase without considering the transformations of a series of intermediate phases and multiple phases.

Small-angle X-ray scattering (SAXS) is a powerful tool for non-destructively investigating the shape and size distribution of a large number of particles in the bulk sample [20–25]. The combination of SAXS and wide-angle X-ray scattering (WAXS; i.e., X-ray diffraction) was used to study the phase separation of amorphous alloys [26–28]. In this study, we employed simultaneous synchrotron SAXS and WAXS [29,30] to measure the temperature-dependent behavior and various corresponding precipitation steps in Al–5.4 wt%Cu alloy subjected to non-isothermal heating. The concurrent evolutions of lattice structure, volume fraction (growth and dissolution) and structural growths in the thickness and length directions with temperature for various plate-like intermediate precipitates were determined by in situ WAXS and SAXS measurements for the first time. The detailed phase transformation mechanism and structural evolution in the precipitation sequence (comprised of the GP zones and θ″, θ′ and θ phases) can be thus resolved, unlike in previous experimental studies. Our data analysis also considered the concurrent existence and transformation of θ′ and θ phases (i.e., multiple precipitates) in the precipitation step. Moreover, the evolutional behaviors of the orientation and spatial distribution of precipitates relative to the lattice planes of the Al matrix during each precipitation step are concurrently determined from our in situ two-dimensional (2D) SAXS patterns. Due to the distinctive SAXS profiles contributed by the GP zones (spatially ordered), θ″ and θ′ phases, different SAXS analysis models were proposed herein to successfully interpret the SAXS data.

The in situ SAXS and WAXS measurements characterizing the concurrent evolutions of lattice phase, morphology and spatial orientation can determine whether the new phase is nucleated from another site or is formed by the transformation of the precursor into a nucleation site. In the present study, the new information provides insight into the phase transformation mechanism of non-isothermal precipitation for the aluminum alloys. The phase transformations and morphological behavior of a series of metastable intermediate precipitates are correlated with a simple non-isothermal precipitation kinetics theory herein. The results advance the current fundamental understanding of this process. These data can serve as the basis for modifying or improving future theoretical studies. Finally, this study is relevant to industrial applications because several important processes and treatments are non-isothermal, such as welding.

2. Experimental

The 2-mm-thick Al–5.4 wt%Cu alloy sheets were fabricated by ALCAN International. The composition of impurity of the alloy is listed in Supplementary data. The alloy sheets were heat-solution treated at 542 °C and then drop-quenched in water at room temperature (RT). Before the SAXS/WAXS experiment, one alloy sample was aged at RT for one month (i.e., naturally aged) and another was aged at 200 °C for 1 h, respectively. These samples are denoted as NA and A1h, respectively, for simplification. The simultaneous SAXS/WAXS experiment was performed at the National Synchrotron Radiation Research Center, Taiwan. The experimental procedure and scattering instrument configuration (see Fig. 1) were described elsewhere [29]. The optimum thickness for the Al–Cu samples is ~200 μm. The grain size in the alloy samples observed by the optical microscope is averagely 120 μm. The beam size (~1 mm^2) allows us to probe the precipitates lying on several oriented grains (like powder-like sample). The sample being studied was placed in a program-controlled heating container. In situ SAXS/WAXS measurements were conducted to study the precipitation behavior during heating from RT to 500 °C for the NA and A1h samples. The heating rate for both samples was 20 °C/min. The 2D SAXS and WAXS patterns collected were reduced into 1D SAXS and WAXS profiles as a function of the scattering vector, Q (=$4\pi/\lambda\sin(\theta/2)$; θ is the SAXS scattering angle, λ is the incident radiation wavelength), respectively, using standard data reduction procedures (e.g., background subtraction, angular averaging). Because the SAXS and WAXS data collection times per frame differed, the measured temperatures were slightly shifted between the SAXS and WAXS data.

3. Results

The temperature-dependent 1D WAXS patterns of the samples after natural aging (NA) or artificial aging (A1h) pretreatment during non-isothermal heating are shown in Fig. 2. The theoretical X-ray diffraction (XRD) patterns of the θ″, θ′, θ and α matrix phases in the Al–Cu alloy were calculated using Powder Cell software (see Supplementary data). The peak positions and relative intensities of the experimental WAXS patterns corresponding to the θ″, θ′, θ and α matrix phases (Fig. 2) are consistent with the theoretical XRD patterns. The temperature dependence of the peak positions in the WAXS patterns during heating signifies the phase (lattice structure) transformation between the intermediate phases of each step in the precipitation sequence. For the NA sample (Fig. 2a), the precipitation sequence identified by WAXS is as follows: GP (RT ~ 210 °C) → θ′ (210–390 °C) → θ′ + θ (390–450 °C) → θ (450–510 °C). For the A1h sample (Fig. 2b), the corresponding precipitation sequence is as follows: θ″ (RT ~ 270 °C) → θ′ (270–350 °C) → θ′ + θ (350–410 °C) → θ (410–510 °C). The temperatures and WAXS peak positions of the various phases are listed in Tables S1 and S2 of the Supplementary data. Moreover, the temperature evolution of the relative peak intensities in the WAXS patterns qualitatively indicates the dissolution or growth of the precipitate phase in each step. According to the WAXS result, we can describe the precipitation sequence more definitely and generally than previous reports: (1) dissolution of the θ″ (GP II zones) or GP zones (formed in the pretreatment) → (2) formation and growth of the θ′ phase → (3) dissolution of θ′ concurrently with the formation of the θ phase → (4) growth of only the θ phase (also see Table S1). This information is reported for the first time based on direct evidence from in situ structural characterization. The 2D WAXS patterns corresponding to (1) the initial GP zones, (2) the initial θ″ phase, (3) the intermediate θ′ phase, (4) the concurrent existence of the θ′ and θ phases and (5) the final stable θ phase are demonstrated in Fig. 3.

Simultaneous SAXS measurements were conducted to correlate the phase transformation to the concurrent morphological

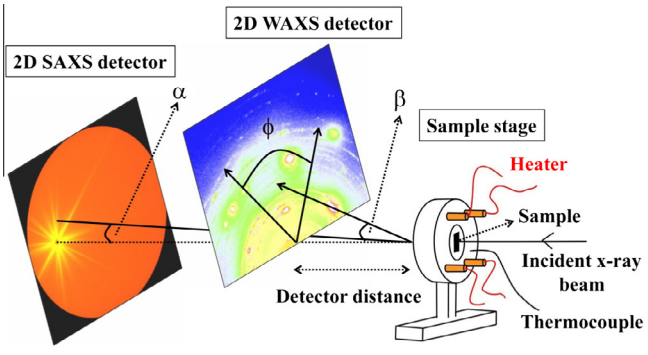

Fig. 1. Instrumental configuration of simultaneous SAXS/WAXS measurement.

Author's personal copy

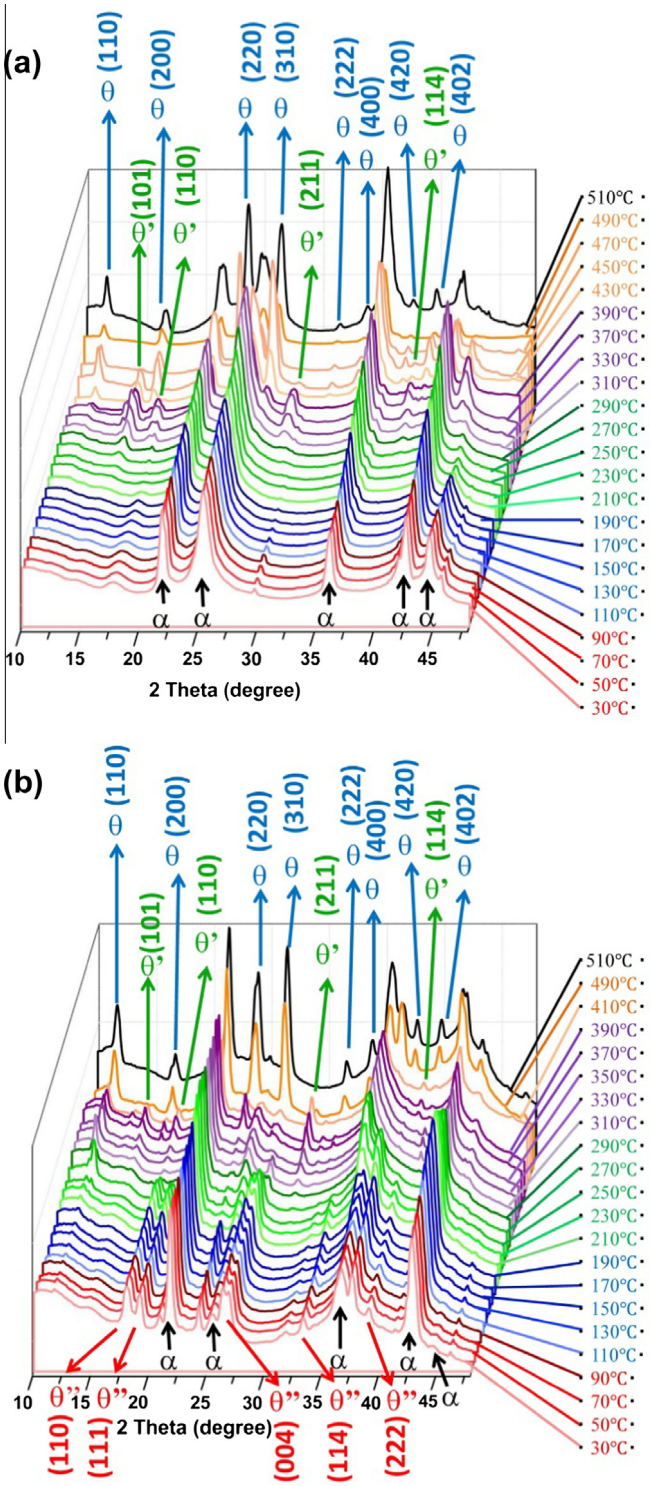

Fig. 2. Variation of WAXS patterns with temperature during the heating process for the (a) naturally aged sample (NA) and (b) artificially aged sample (A1h).

evolution of precipitates to provide a comprehensive understanding of the process. Temperature-dependent SAXS profiles of the naturally and artificially aged samples were obtained concurrently with WAXS measurements during the heating process, as shown in Fig. 4. The volume fraction, radius and thickness of the precipitates can be quantitatively determined by SAXS model analysis. The variation in the shape and intensity of the SAXS profiles (Fig. 4) shows the structurally distinctive evolution of precipitates (growth, dissolution and aspect ratio) during heating, signifying different precipitation sequences. The SAXS profiles of the naturally aged sample corresponding to the GPZ phase (RT ~ 193 °C), the θ′ phase (193–338 °C) and the θ′ → θ phase (317–462 °C) are shown in Fig. 5 as representative examples. It is well-known that the various precipitates in Al–Cu alloys identified by TEM studies are plate- or disk-like. The SAXS profile of the disk-like precipitates can be expressed by the form factor of a cylinder, $P(Q)$ [20,23,31], with a radius, R, and thickness, t, as given by

$$I(Q) = N_P P(Q) = \eta \Delta\rho^2 (\pi R^2 t) \int_0^{\pi/2} \left[2j_0\left(\frac{Qt}{2}\cos\alpha\right) \frac{j_1(QR\sin\alpha)}{(QR\sin\alpha)} \right]^2 \times \sin\alpha \, d\alpha \quad (1)$$

where N_P and η are the particle number density and volume fraction of plate-like cylinder, respectively, in the sample. $\Delta\rho$ denotes the scattering length density contrast of the cylinder. The integral over α averages the form factor over all possible orientations of the cylinder with respect to Q. The product of $\Delta\rho$ and η can be regarded as a prefactor. The determination of the absolute η value is affected by the $\Delta\rho$ value used in the non-linear least squares calculation. The $\Delta\rho$ values of the θ″, θ′ and θ phases calculated according to the respective lattice structures are 0.83, 1.05 and 1.23×10^{-5} Å^{-2}, respectively. However, the $\Delta\rho$ values for all phases in this study are set as 1.05×10^{-5} Å^{-2} when determining the relative volume fraction to simplify the discussion.

The GPZ phase forms during quenching (quenched-in precipitates) or RT aging. The SAXS profile of GPZ, shown in Fig. 5a, has a characteristic structure peak at $Q = \sim 0.1$ Å^{-1} due to the interaction between particles. This structure peak implies low ordering of the spatial distribution of GPZ. Accounting for inter-particle effects, Eq. (1) is extended as

$$I(Q) = N_P P(Q) \cdot S(\eta, Q) \quad (2)$$

where $S(Q)$ is a structure factor that can be described by the hard-sphere model. Our previous studies show that the hard-sphere structure factor calculated by the Percus–Yevick approximation can be successfully used to model the precipitates in Al–Li alloys [32–34]. This hard-sphere structure factor is adopted in Eq. (2). In contrast, during the initial heating stage, power-law scattering behavior (i.e., $I(Q) \propto Q^{-4}$) exists in the low-Q region (Figs. 5a and 4) due to the sharp boundary of large impurity precipitates. Excluding the effect of these large particles, the measured SAXS profiles can be modeled by

$$I(Q) = AQ^{-4} + N_P P(Q) \cdot S(\eta, Q) = AQ^{-4} + \frac{\eta}{(\pi R^2 t)} S(\eta, Q) \cdot P(Q) \quad (3)$$

where A is a constant. Eq. (3) is denoted as Model (I). The SAXS profiles corresponding to the GPZ phase can be fitted using Model (I), as shown in Fig. 5a. The position of the structure peak shifts toward the low-Q region with increasing temperature, evidencing the structural evolution of GPZ. The structural parameters extracted by this SAXS analysis are listed in Table 1. For avoiding too many free parameters in the modeling of structure factor, we ignore the consideration of polydispersity of diameter, which would cause some uncertainty of mean diameter

The characteristic shape of the SAXS profiles changes upon heating to 213 °C (Fig. 5b). The low-Q intensities increase significantly due to the dramatic growth of the size and volume fraction of the particles, indicating that power-law scattering (which is a contribution of the impurity phase) can be ignored. The corresponding WAXS patterns consistently demonstrate the transformation of the lattice phase into the θ′ phase. To accurately model the SAXS profiles, the form factor of polydispersed cylinders with a Schulz distribution of the thickness is used because it provides

Author's personal copy

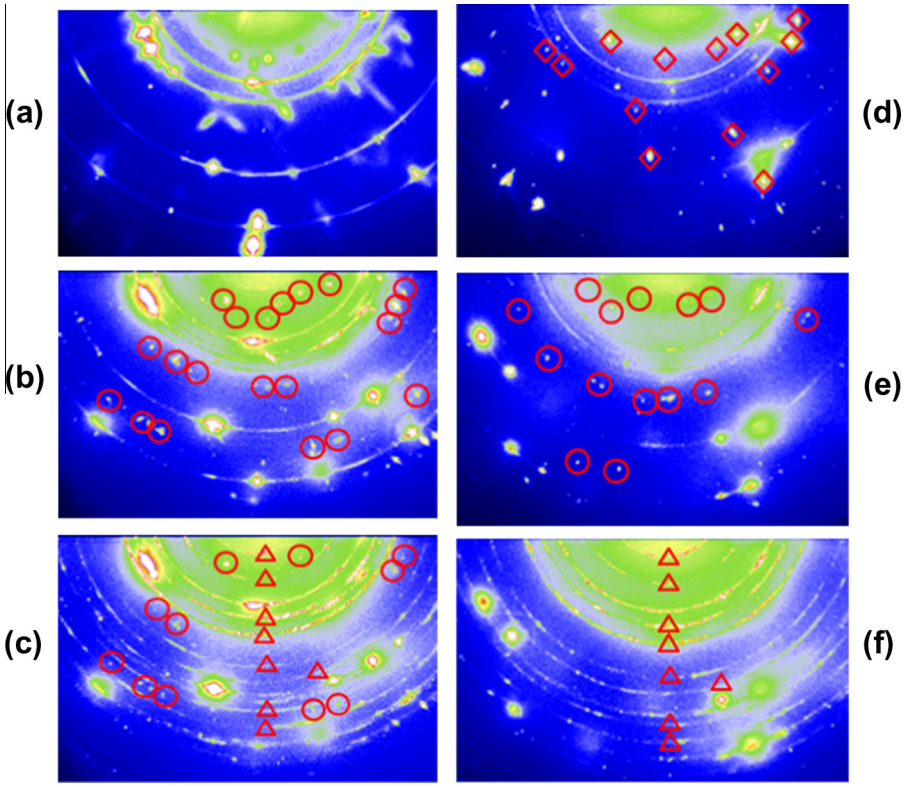

Fig. 3. 2D WAXS patterns corresponding to the 1D WAXS patterns of the NA sample at (a) RT (GP zones), (b) 370 °C (θ′) and (c) 450 °C (θ′ + θ) and the A1h sample at (d) RT (θ″), (e) 350 °C (θ′) and (f) 510 (θ). The GP zones are difficult to observe. The θ″ phase, θ′ phase and XRD rings of the θ phase are marked by diamonds, circles and triangles, respectively.

a better fit than the other models. The SAXS profile for this polydispersed system can be expressed as

$$I(Q) = \frac{\eta}{(V_P)} \cdot \Delta\rho^2 \cdot \int_0^x \times \int_0^{\pi/2} \left[2(\pi R^2 t) f(t) j_0\left(\frac{Qt}{2}\cos\alpha\right) \frac{j_1(QR\sin\alpha)}{(QR\sin\alpha)} \right]^2 \times \sin\alpha \, d\alpha \, dt \quad (4)$$

where $f(t)$ is the normalized Schulz distribution of the thickness and V_p is the mean volume of polydispersed cylinders. The polydispersity of the thickness is related to σ/t_{avg} (σ is the variance of the Schulz distribution; t_{avg} is the mean thickness) [35]. Eq. (4) is denoted as Model (II). The SAXS profiles corresponding to the θ′ or θ phase ($T \geqslant 213$ °C) can be fitted by Model (II), as shown in Fig. 5b and c. The structural parameters extracted by Model (II) are listed in Table 1. The polydispersity determined by SAXS analysis is ~0.35. In this case (plate precipitate with large diameter), the lowest scattering vector (relate to the size range of diameter) is not enough to give an accurate estimation of the polydispersity in the diameter distribution. For avoiding too many parameters and erroneous polydispersity of diameter, we ignore the distribution of diameter.

The SAXS profiles of the artificially aged sample (A1h) at $T \leqslant 267$ °C during heating are relatively stable (Fig. 4b). The corresponding WAXS pattern consistently indicates that the lattice phase is a pure θ″ phase (i.e., GP II zone). When the heating temperature is above 267 °C, the shape of the SAXS profiles (related to the morphology) varies remarkably with temperature. The corresponding WAXS patterns show that the θ′ phase transformed immediately from the θ″ phase (Fig. 2b). For modeling the θ″ phase precipitates formed in the pretreatment and excluding the effect of large impurity particle, the SAXS intensity can be expressed as

$$I(Q) = AQ^{-4} + \frac{\eta}{(\pi R^2 T)} \cdot P(Q) \quad (5)$$

Eq. (5) corresponds to Eq. (3) with assuming $S(Q) \sim 1$ and called Model (III) here. The SAXS profiles corresponding to the θ″ phase of the A1h sample can be fitted using the Model (III), as shown in Fig. S3. The SAXS profiles corresponding to θ′ or θ phase are also fitted well using the Model (II) (similar to the case of the NA sample). The structural parameters extracted by SAXS Model (II) for the A1h sample are listed in Table 2.

Previous TEM studies have indicated that the plate-like precipitates have (0 0 1) θ′//$\{0\,0\,1\}_{\alpha\text{-Al}}$ interfaces parallel to their broad faces. The in situ measurement is particularly well suited to investigate the formation of the GPZ, θ″, θ′ and θ phase precipitates on the {1 0 0} planes of the matrix and the evolution of their orientation with phase transformation and morphological variation in the precipitation sequence. The in situ 2D SAXS patterns in this study can provide insight into the orientation of various precipitates. A series of 2D SAXS patterns for the NA and A1h samples during heating (before reduction into the 1D SAXS profiles in Fig. 4) are available in the Supplementary data. Regarding the difference in the precipitation sequence between the samples, the representative 2D SAXS patterns are shown in Fig. 6. For the NA sample, the 2D SAXS patterns (30–210 °C) corresponding to the GPZ phase (the SAXS profile in Fig. 5a) show no apparent features (e.g., anisotropy) because its volume fraction is too small. The 2D SAXS patterns (230–330 °C) corresponding to the formation and growth of the θ′ phase include several weak cross-like shapes, which then gradually increase in size and intensity. Each cross-like shape (comprising the radial streaks [36,37]) is caused by the scattering

Author's personal copy

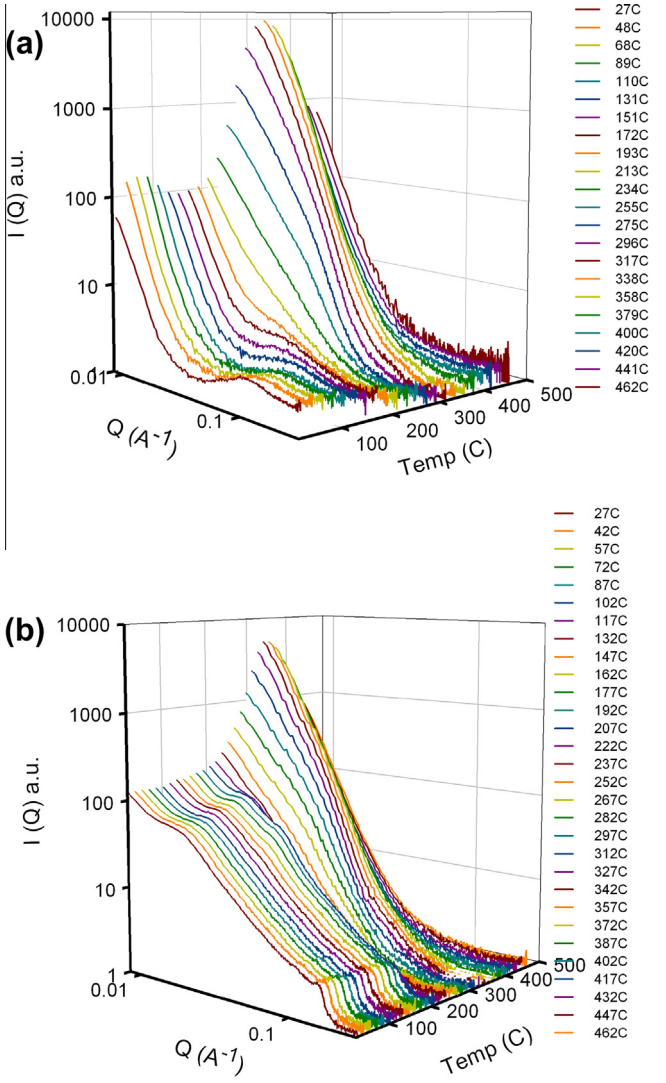

Fig. 4. Variation of SAXS profiles with temperature during the heating process for the (a) naturally aged sample (NA) and (b) artificially aged sample (A1h).

of plate-like particles lying on the {1 0 0} planes of the matrix in a grain, depending on the orientation of this matrix grain relative to the incident synchrotron beam. This evolutional orientation behavior can be observed visually and is consistent with the corresponding SAXS/WAXS interpretations based on the structural evolution (growth in volume fraction and size) (Fig. 5b and Table 1) and the phase identification (Fig. 2). Similarly, the shrinkage of the 2D SAXS patterns (330–430 °C) reveals the morphological growth. The literatures [36,37] reported that the similar radial streaks in the 2D SAXS pattern are from the scattering of the plate-like precipitates in a single crystal or an orientated grain of polycrystalline materials. The thickness and length of plate-like precipitates can be accurately determined by the profiles slicing along and across the corresponding streaks, respectively. For the 2D SAXS pattern from a grain with a certain orientation, the direct analysis of streak intensity can provide high resolution of structural characterization. Our work roughly studies the global effect cause by all possible orientations of precipitates. The integration of intensity over some or few orientations may cause a certain degree of uncertainty. The resolution is also limited due to the lowest scattering vector compared to the direct analysis of the streak intensity.

In contrast, the cross-like shapes (or radial streaks) in the 2D SAXS patterns of the A1h sample (30–250 °C) corresponding to the θ″ phase (also identified by WAXS) are broad-band bars, implying extreme thinness and possibly a slight distribution of the orientation relative to the {1 0 0} planes. There are relatively few crosses, indicating a somewhat spatially heterogeneous distribution along the preferable zone (or grain). This interpretation is supported by the weak structure peak at high Q (=0.16 Å^{-1}) in the corresponding 1D SAXS profiles (Fig. 4b). This structure peak (neglected in the SAXS model fitting due to its relative insignificance) represents a local short-range ordering of the precipitate distribution. Similarly, the 1D SAXS profiles corresponding to GP zones (Fig. 4a) also exhibit a structure peak. A locally heterogeneous distribution is suggested based on these common features. In the subsequent transformation into the θ′ phase (270–370 °C), the edge-on precipitates lying on the habit planes from more grains are demonstrated on the 2D SAXS pattern by the increasing number of streaks.

4. Discussion

Simultaneous, independent SAXS and WAXS (or XRD) measurements can provide complementary information about the phase transformation and structural evolution in precipitation sequences with different pretreatments, as discussed in Section 3. Tables 1 and 2 list the parameters determined by the appropriate SAXS models established due to the different structural characteristics of precipitates for comparison with the lattice structures, growth and dissolution of the phases predicted by WAXS measurements at the same elevated temperatures. Based on the SAXS analysis, the evolutions of the relative volume fraction, diameter and thickness with heating temperature are shown in Figs. 7–9, together with the phase. A detailed discussion is presented as follows.

4.1. Precipitation in the naturally aged Al–Cu alloy during heating

The GPZ (Cu-rich plate-like cluster) thickness determined by SAXS, 2.4 Å, corresponds to approximately one atom, which is consistent with previous reports [1,3,4,10]. Because of the thin geometry (atomic layers) of the GPZ, WAXS cannot produce a clear pattern. During the dissolution of GPZ (RT ∼ 213 °C), the relative volume fraction gradually decreases. However, the diameter increases (possibly due to particle coalescence) from 16 to 160 Å with an almost fixed thickness during this dissolution step. The size (diameter) range determined by SAXS analysis agrees with that reported by another study [10]. The dissolution behavior (in volume fraction) and concurrent distinctive diameter and thickness changes are quantitatively reported in detail. These findings roughly agree with the theoretical prediction of non-isothermal precipitation kinetics (which will be discussed in Section 4.3).

When the heating temperature exceeds 213 °C, the lattice phase of the full precipitates is quickly transformed into the θ′ phase. Their relative volume fraction, diameter and thickness also increase significantly until reaching the maximum volume fraction (=0.0623), which is attained at T = 338 °C (Table 1 and Figs. 7–9). This step is typical for the θ′ phase, as evidenced by both SAXS and WAXS measurements. It is reasonable to suspect that the residual GP zones remaining after the last step are highly likely to function as the nuclei of the θ′ phase. Starting at 338 °C, the relative volume fraction begins to decrease dramatically (Fig. 7), which is also evidenced by the reduction in the peak intensities of the θ′ phase (WAXS patterns). Thus, the step from 358 to 441 °C can be defined as the dissolution of the θ′ phase. Note that the diameter of the θ′ precipitates remains constant, whereas their thickness continues to increase and eventually plateaus. It is apparent that the θ′ precipitates continuously thicken during the growth and dissolution processes. During the θ′-dissolution step, the morphology (global size) of the θ′ precipitates continues to

Author's personal copy

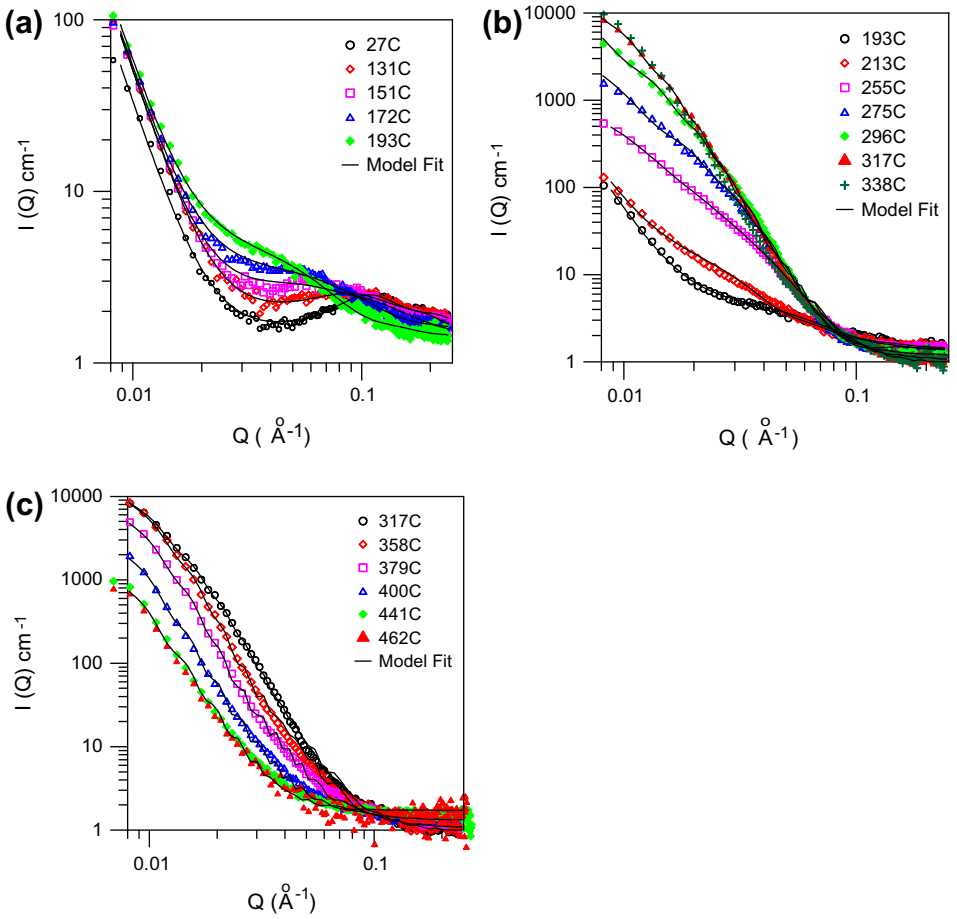

Fig. 5. Temperature-dependent SAXS profiles of the naturally aged sample during heating, recorded at (a) RT ~ 193 °C (GPZ phase), (b) 193–338 °C (primarily the θ′ phase) and (c) 317–462 °C (θ′ → θ phase). These SAXS profiles are well fitted by the respective SAXS analysis models. (The error bars for the SAXS data are less than 1% in the low-Q region and gradually increase with Q up to ~3% at $Q = 0.1$ Å^{-1}.)

Table 1
Structural parameters determined by the SAXS models and the phase status predicted by WAXS for the NA sample.

Temp. (°C)	Rel. η	Radius (Å)	Thickness	SAXS model	Phase status*
27	0.0020	8.2	2.4	I	GPZ (s)
48	0.0021	7.6	2.4	I	GPZ (s)
131	0.0014	10.2	2.4	I	GPZ (d)
151	0.0006	16.2	2.4	I	GPZ (d)
172	0.0004	24.5	2.4	I	GPZ (d)
193	0.0003	37.3	2.4	I	GPZ (d)
213	0.0001	82.8	7.3	I	GPZ (d)
234	0.0053	234.2	37.8	II	θ′ (f)
255	0.0100	220	56.0	II	θ′ (f)
275	0.0210	301.3	73.7	II	θ′ (f)
296	0.0413	422.4	109.0	II	θ′ (f)
317	0.0600	564.3	154.4	II	θ′ (f)
338	0.0623	557.9	192.9	II	θ′ (f)
358	0.0493	565.2	216.5	II	θ′ (d)
379	0.0270	580.1	235.9	II	θ′ (d)
400	0.0103	588.0	259.4	II	θ′ (d)
420	0.0063	578.5	248.7	II	θ′ (d)
441	0.0053	604.7	241.8	II	θ′ (d), θ (f)
462	0.0031	512.2	154.7	II	θ (f)

* Predicted by the WAXS patterns; (s): stable, (d): dissolution, (f): formation, and (o): lattice ordering.

Table 2
Structural parameters determined by the SAXS models and the phase status predicted by WAXS for the A1h sample.

Temp. (°C)	Rel. η	Radius (Å)	Thickness (Å)	SAXS model	Phase status*
27	0.065	85.4	14.6	III	θ″ (s)
57	0.067	85.4	14.3	III	θ″ (s)
87	0.066	85.6	14.7	III	θ″ (s)
117	0.067	88.6	14.8	III	θ″ (s)
147	0.069	87.3	14.9	III	θ″ (s)
192	0.069	87.8	17.5	III	θ″ (s)
222	0.032	103	18.6	III	θ″ (d)
252	0.027	110	18	III	θ″ (d)
267	0.019	106.2	44.5	III	θ″ (d)
282	0.029	290	70.1	II	θ′ (f)
297	0.038	291.4	90.6	II	θ′ (f)
312	0.052	286.5	117.5	II	θ′ (f)
327	0.065	284.6	147.6	II	θ′ (f)
342	0.073	279.3	171.2	II	θ′ (f)
357	0.069	271.9	182.9	II	θ′ (f)
372	0.057	262.7	187.5	II	θ′, θ (f)
387	0.043	299.7	193.9	II	θ′, θ (f)
402	0.026	299.7	200.5	II	θ′ (d), θ (f)
417	0.017	311.5	211	II	θ (f)
432	0.013	304.1	203.4	II	θ (f)

* Predicted by the WAXS patterns; (s): stable, (d): dissolution, (f): formation, and (o) lattice ordering.

grow, albeit slowly. This distinctive growth differs from the behavior predicted by isothermal aging. Because knowledge of non-isothermal heating is currently very limited and more complex, we present this distinctive experimental finding as the basis for future theoretical study. The initial thicknesses of the θ′ precipitates (3.7–5.6 nm) are similar to those observed by another TEM study for isothermally aged Al–Cu alloys [5]. The diameters of the θ′

Author's personal copy

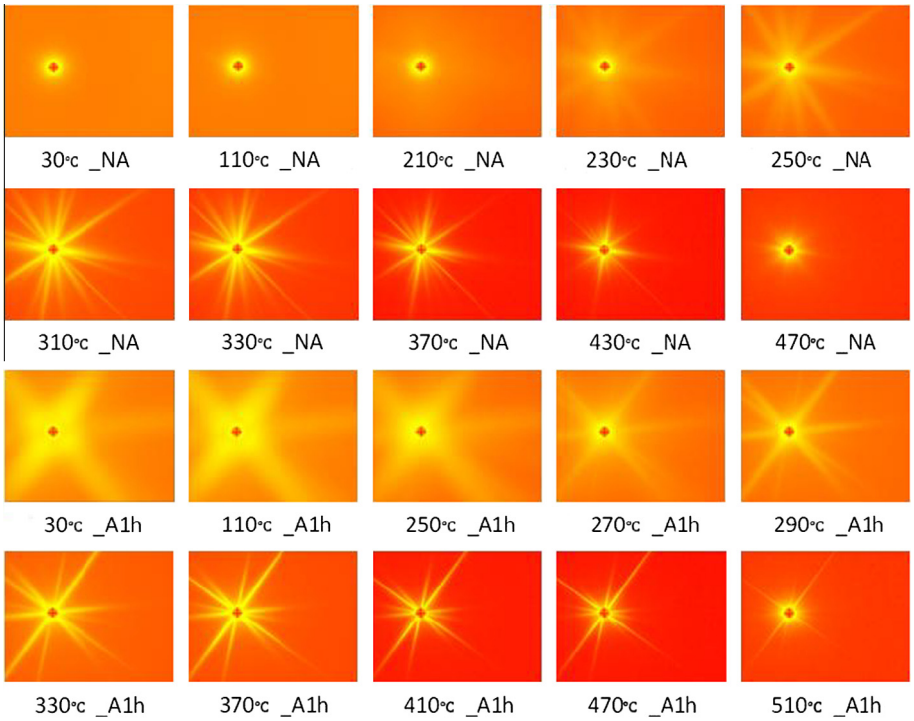

Fig. 6. Representative two-dimensional SAXS patterns showing the orientation and spatial distribution of intermediate phases in the precipitation sequences during the heating process for the NA and A1h samples. (Bright color represents the high intensity.) (For interpretation of the references to color in this figure legend, the reader is referred to the web version of this article.)

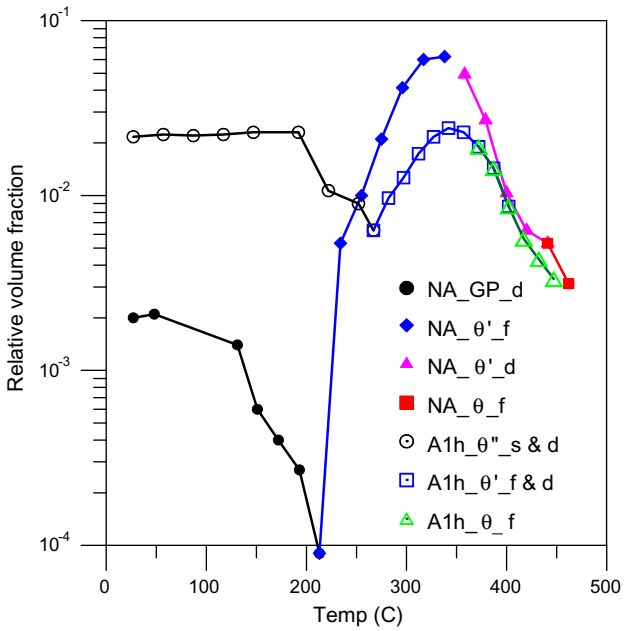

Fig. 7. Evolution of the relative volume fraction with heating temperature in the precipitation sequence, with each intermediate-phase step noted. (f): formation. (d): dissolution.

precipitates reported herein are 50–100 nm, which are also similar to those obtained by other TEM studies [5,6]. In Table 1, the final θ′ precipitates formed by non-isothermal heating are thicker (~25 nm) than those produced by isothermal aging.

Moreover, the WAXS measurement also indicates that the θ phase forms concurrently from 430 °C (Fig. 2a and Table S1). The penultimate stage of the θ′-dissolution step (430–450 °C for WAXS) corresponds to the coexistence of both θ′ and θ phases (i.e., θ′ dissolution concurrent with θ formation). As shown by the SAXS measurement (430–441 °C), the volume fraction decreases in this stage. The morphology (size) characterized by SAXS continues to increase slightly (or plateaus) and does not exhibit a bimodal size distribution. The θ′ precipitates may serve directly as nuclei, with the gradual transformation of the lattice structure into the θ phase as the primary action in the penultimate stage.

When the heating temperature exceeds 450 °C, only the θ phase exists, as evidenced by the WAXS pattern. This step is usually considered to be the formation of the θ phase. The peak intensities of the θ phase in the WAXS patterns increase with increasing temperature during this step, whereas the corresponding volume fraction determined by SAXS continues to decrease and the global size begins to shrink (Figs. 7–9). The volume fraction and global size measured by our SAXS during this step is not true and can be explained by the fact that a significant proportion of the intensity scattered at very small angles is lost into the beam stop. It leads to the failure of SAXS analysis. The intensity increase of the corresponding WAXS patterns would be interpreted as the growth (formation) of stable θ phase. The behaviors of the concurrent lattice transformation and structural evolutions in different directions cannot be resolved by conventional DSC analysis [15–17] for Al–Cu alloys, which assumes that the growth and dissolution steps are separate and ignores structural evolution.

4.2. Precipitation in the artificially aged Al–Cu alloy during heating

During heating from RT to 267 °C, only the θ″ phase (i.e., GP II zones) exists, as evidenced by the WAXS patterns (Fig. 2 and Table S2). The corresponding SAXS analyses show that the substep during RT ~ 192 °C has a stable volume fraction (~0.07), diameter (~17 nm) and thickness (~1.5 nm), indicating thermal stability. The diameter and thickness of the θ″-phase precipitates are similar to those reported by the other TEM measurement of θ″-phase

Author's personal copy

precipitates (21.8 and 2.02 nm, respectively) [3]. The thickness is also close to that of the early-stage θ′-phase precipitate measured in other TEM studies (~2 nm) [6,7]. This substep (RT ~ 192 °C) is referred to as the stable state of the θ″ phase. The following substep, 192–267 °C, is then referred to as the dissolution of the θ″ phase because its volume fraction decreases substantially, as determined by SAXS analysis (Table 2). Note that the diameter gradually grows with an almost fixed thickness during the dissolution step. These behaviors are similar to those in the dissolution step of GP zones mentioned in Section 4.1 (Table 2 and Figs. 7–9).

When the heating temperature exceeds 267 °C, the WAXS patterns exhibit the disappearance of the θ″ phase, immediately followed by the formation and growth of the θ′ phase (Fig. 2 and Table S2). The θ′ phase exists in the step from 282 to 402 °C. The SAXS analysis (Table 2) demonstrates that the volume fraction of θ′ precipitates increases until the maximum value at 342 °C (i.e., θ′ growth step) and then decreases from 342 to 402 °C (i.e., θ′ dissolution step). During the growth and dissolution of θ′ (282–402 °C), the diameter promptly grows to ~60 nm at the starting time and then keep stable. However, the thickness linearly increases regardless of growth and dissolution (Figs. 8 and 9). This situation is also similar to thickening of the θ′ precipitates in the case of the naturally aged sample. In contrast, the thickness and diameter of θ′ precipitates in the A1h sample is much less than those in the NA sample. The reason may be that the θ″ phase well formed in the pre-treated A1h sample exhaust and largely change the distribution of solute Cu atoms, inhibiting the growth of the following θ′ precipitates. The WAXS patterns also indicate the formation of θ phase starting from 370 °C. The θ′ and θ phases coexist during the period from 387 to 402 °C. During this period, the SAXS profiles demonstrate these two phase keep the same morphology, indicating that the only transformation of the lattice structure (θ′ → θ) proceeds in the precipitates. Here, the quantitative and qualitative behaviors for the θ′ → θ phase transformation are similar to those for the NA sample. The reproducibility among different samples testifies to the validity of our data.

Finally, the growth or formation of the single θ phase begins at above 402 °C is evidenced by the WAXS patterns. This step is the formation of the θ phase. The volume fraction and global size of

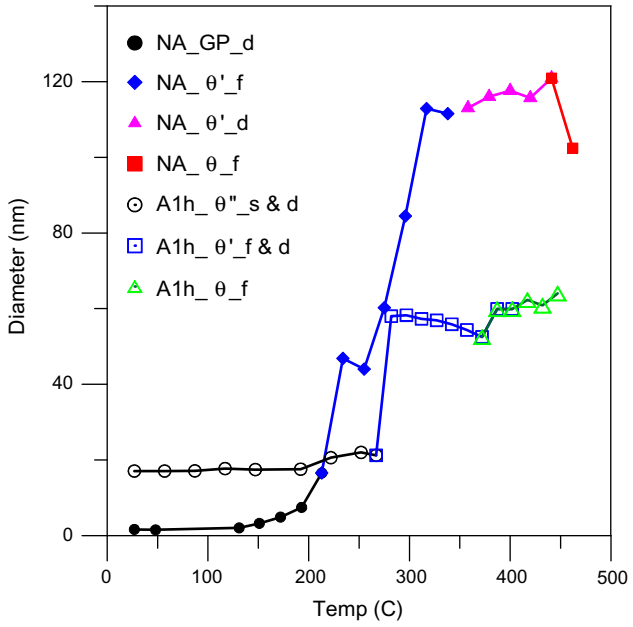

Fig. 8. Concurrent evolution of the diameter with heating temperature, corresponding to Fig. 6.

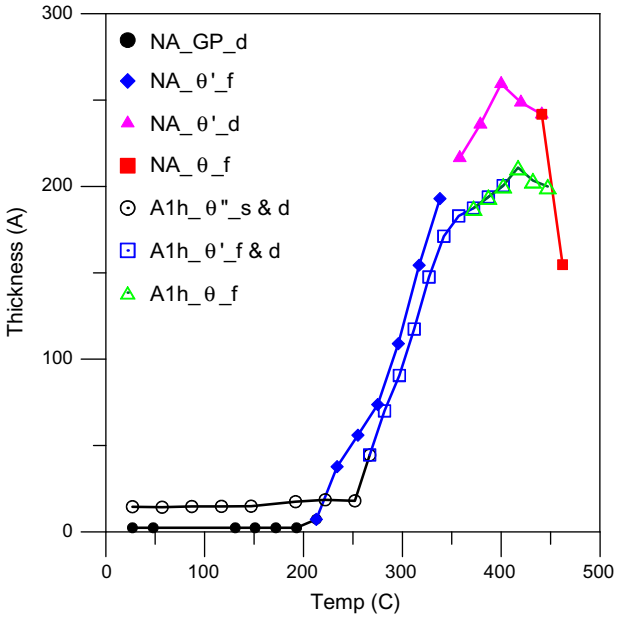

Fig. 9. Concurrent evolution of the thickness with heating temperature, corresponding to Fig. 6.

the precipitates determined by the SAXS profiles (Table 2 and Figs. 7–9) are wrong due to the same reason of the NA sample in the high-temperature step (i.e., a loss of low-*Q* scattering intensity caused by the dramatic increase and growth of θ particles).

4.3. Correlation between non-isothermal precipitation model and experimental SAXS/WAXS results

To date, there is no theoretical model that describes the non-isothermal precipitation coupled with the complex lattice transformations of a sequence of intermediate (metastable) phases and the associated morphological evolution. A theoretical model of non-isothermal precipitation describing the behavior (in volume fraction and global size) of a single metastable precipitate directly transformed into a stable precipitate during heating was previously developed and successfully calibrated using experimental data for Al–Zn–Mg alloy [38]. For simply, we adopted this model to interpret some of the local behaviors (for each step) resulting from the lattice transformations of multiple intermediate phases. Our result not only qualitatively agrees with the model description but also provides a comprehensive understanding of the complex mechanism involved in the precipitation sequence. The volume fractions of the GP zones and θ″ phase begin to decrease rapidly after the heating temperature exceeds the point of thermal stability (50 and 190 °C, respectively). The model refers to this stage as the dissolution step. After passing these minimum values, the volume fractions increase rapidly to near-saturation (see Fig. 7). In the same period, their global sizes are initially fairly stable and then grow rapidly or coarsen (Figs. 8 and 9). It (GPZ or θ″ → θ′) agrees well with the model predictions for the reversion process with ramp heating (Figs. 2, 3 and 7 of [38]). The model predicts that the global size will begin to grow (in volume fraction) toward the end of the dissolution stage. The model attributes this growth to the mean radius being larger than the critical radius. The model also notes that the minimum volume fraction is related to a phase transformation from metastable precipitates to stable ones.

The reason why the saturation of volume fractions (at 300–350 °C) is followed by a rapid dissolution during heating (see Fig. 7; θ′ → θ) is as follows. This theoretical model predicts

Author's personal copy

that, under continuous heating to high temperatures, the volume fraction naturally decays. The theoretical model also predicts a temporary interruption behavior or inflexion point (competition between dissolution and growth of particles), especially for the slow heating rate of 10 °C/min and T6 temper (Figs. 5 and 13 of [38]). A similar temporary interruption behavior (the increase of the volume fraction followed by saturation) was observed between 250 and 350 °C in this study. From a thermodynamics viewpoint, for low heating rates or certain pretreatments, such as that used here, there exists a lower critical radius (close to the mean radius), leading to a short coarsening (in size) stage with a saturation volume fraction [38]. When the temperature becomes very high, the critical radius increases again and dissolution resumes. This theoretical model cannot fully and quantitatively explain our SAXS/WAXS results because of the effect of multiple lattice transformations (or morphologies with high aspect ratios) in the sequence. Although this discrepancy still exists, the cross-examination between theory and experiment herein indicates self-consistency. The theoretical model and our experimental results complementarily provide a comprehensive understanding of the mechanisms involved.

5. Conclusion

For the Al–Cu alloy systems, the transformation of the phase lattice structure and concurrent structural changes of the volume fraction (growth and dissolution), orientation and growth in the thickness and length directions with heating temperature for intermediate precipitates were accurately and simultaneously determined by in situ WAXS and SAXS measurements (direct structural measurements). The relationship between these structural parameters is new information. The precipitation behavior in the sequence can be refined into the following steps: (1) dissolution of the θ″ or GP zones (formed by the pretreatment), (2) formation and growth of the θ′ phase, (3) dissolution of the θ′ phase, in which the formation of θ phase concurrently occurs in the late period, and (4) growth of the pure θ phase. The quantitative information provided herein furthers the understanding of the phase transformation mechanisms in the precipitation sequence and theoretical modeling.

Acknowledgements

We appreciate Prof. S. Esmaeili (University of Waterloo, Canada) for providing the Al–Cu samples and useful suggestions. EW-H appreciates the financial support from National Science Council (NSC) 101-2221-E-008-039-MY3 Program. MH-W thanks the NSC-102-3113-P-007-014 Program.

Appendix A. Supplementary material

Supplementary data associated with this article can be found, in the online version, at http://dx.doi.org/10.1016/j.jallcom.2013.04.201.

References

[1] S.Y. Hu, M.I. Baskes, M. Stan, L.Q. Chen, Acta Mater. 54 (2006) 4699.
[2] L. Bourgeois, C. Dwyer, M. Weyland, J.F. Nie, B.C. Muddle, Acta Mater. 59 (2011) 7043.
[3] A. Biswas, D.J. Siegel, C. Wolverton, D.N. Seidman, Acta Mater. 59 (2011) 6187.
[4] H. Sehitoglu, T. Foglesong, H.J. Maier, Metall. Mater. Trans. A 36 (2005) 749.
[5] J.F. Nie, B.C. Muddle, Acta Mater. 56 (2008) 3490.
[6] A.W. Zhu, J. Chen, E.A. Starke Jr., Acta Mater. 48 (2000) 2239.
[7] L. Bourgeois, C. Dwyer, M. Weyland, J.F. Nie, B.C. Muddle, Acta Mater. 60 (2012) 633.
[8] Y. Li, G. Purdy, Acta Mater. 56 (2008) 364.
[9] V. Vaithyanathan, C. Wolverton, L.Q. Chen, Acta Mater. 52 (2004) 2973.
[10] K. Osamura, Y. Murakami, T. Sato, T. Takahashi, T. Abe, K. Hirano, Acta Metall. 31 (1983) 1669.
[11] K. Osamura, N. Otsuka, Y. Murakami, Philos. Mag. 45 (1982) 583.
[12] T.J. Konno, K. Hiraga, M. Kawasaki, Scripta Mater. 44 (2001) 2303.
[13] M. Takeda, Y. Maeda, A. Yoshida, K. Yabuta, S. Konuma, T. Endo, Scripta Mater. 41 (1999) 643.
[14] A.M. Zahra, C.Y. Zahra, K. Naviprasad, I.J. Polmear, Philos. Mag. 84 (2004) 2521.
[15] W. Sha, Metall. Mater. Trans. A 37 (2005) 763.
[16] S.K. Son, M. Takeda, M. Mitome, Y. Bando, T. Endo, Mater. Lett. 59 (2005) 629.
[17] M.J. Starink, P. Mourik, Mater. Sci. Eng. A 156 (1992) 183.
[18] S. Esmaeili, D.J. Lloyd, W.J. Poole, Acta Mater. 51 (2003) 3467.
[19] S. Esmaeili, D.J. Lloyd, Acta Mater. 53 (2005) 5257.
[20] O. Glatter, O. Kratky, Small angle X-ray scattering, Academic Press, New York, 1982.
[21] C.S. Tsao, T.L. Lin, M.S. Yu, J. Alloys. Comp. 289 (1999) 81.
[22] C.S. Tsao, U.S. Jeng, C.Y. Chen, T.Y. Kuo, Scripta Mater. 53 (2005) 1241.
[23] C.S. Tsao, C.Y. Chen, U.S. Jeng, T.Y. Kuo, Acta Mater. 54 (2006) 4621.
[24] A. Deschamps, Y. Bre'chet, Acta Mater. 47 (1999) 293.
[25] R. Ferragut, F. Moia, F. Fiori, D. Lussana, G. Riontino, J. Alloys Comp. 495 (2010) 408.
[26] J. Antonowicz, J. Alloys Comp. 434–435 (2007) 126.
[27] J. Antonowicz, M. Kedzierski, E. Jezierska, J. Latuch, A.R. Yavari, L. Greer, P. Panine, M. Sztucki, J. Alloys Comp. 483 (2009) 1116.
[28] E.W. Huang, Y. Liu, Y. Ren, L. Porcar, J.J. Kai, P.K. Liaw, G.S. Smith, W.R. Chen, Philos. Mag. Lett. 91 (2011) 483.
[29] W.R. Wu, U.S. Jeng, C.J. Su, K.H. Wei, M.S. Su, M.Y. Chiu, C.Y. Chen, W.B. Su, C.H. Su, A.C. Su, ACS Nano 5 (2011) 6233.
[30] H.C. Liao, C.S. Tsao, T.H. Lin, M.H. Jao, C.M. Chuang, S.Y. Chang, Y.C. Huang, Y.T. Shao, C.Y. Chen, C.J. Su, U.S. Jeng, Y.F. Chen, W.F. Su, ACS Nano 6 (2012) 1657.
[31] C.S. Tsao, M. Li, Y. Zhang, J.B. Leao, W.S. Chiang, T.Y. Chung, Y.R. Tzeng, M.S. Yu, S.H. Chen, J. Phys. Chem. C 114 (2010) 19895.
[32] C.S. Tsao, C.Y. Chen, J.Y. Huang, Phys. Rev. B 70 (2004) 174104.
[33] C.S. Tsao, T.L. Lin, J. Appl. Crystallogr. 32 (1999) 426.
[34] J.S. Pedersen, J. Appl. Crystallogr. 27 (1994) 595.
[35] S.R. Kline, J. Appl. Crystallogr. 39 (2006) 895.
[36] F.D. Geuser, F. Bley, A. Deschamps, J. Appl. Crystallogr. 45 (2012) 1208.
[37] P. Fratzl, F. Langamayr, O. Paris, J. Appl. Crystallogr. 26 (1993) 820.
[38] M. Nicolas, A. Deschamps, Acta Mater. 51 (2003) 6077.